



HAL
open science

On dynamic behavior of bone: experimental and numerical study of porcine ribs subjected to impact loads in dynamic three-point bending tests

Aravind Rajan Ayagara, André Langlet, Ridha Hambli

► To cite this version:

Aravind Rajan Ayagara, André Langlet, Ridha Hambli. On dynamic behavior of bone: experimental and numerical study of porcine ribs subjected to impact loads in dynamic three-point bending tests. *Journal of the mechanical behavior of biomedical materials*, In press. hal-02137595v1

HAL Id: hal-02137595

<https://hal.science/hal-02137595v1>

Submitted on 23 May 2019 (v1), last revised 28 May 2019 (v2)

HAL is a multi-disciplinary open access archive for the deposit and dissemination of scientific research documents, whether they are published or not. The documents may come from teaching and research institutions in France or abroad, or from public or private research centers.

L'archive ouverte pluridisciplinaire **HAL**, est destinée au dépôt et à la diffusion de documents scientifiques de niveau recherche, publiés ou non, émanant des établissements d'enseignement et de recherche français ou étrangers, des laboratoires publics ou privés.

On dynamic behavior of bone: experimental and numerical study of porcine ribs subjected to impact loads in dynamic three-point bending tests[☆]

Aravind Rajan AYAGARA, André LANGLET*, Ridha HAMBLI

Laboratoire Gabriel Lamé, Univ. Orléans/Univ. Tours/INSA CVL. 63-Av de l'atré de Tassigny, 18020-Bourges, France

Abstract

This study covers the characterization of the dynamic behavior of isolated porcine ribs based on experimental and numerical approaches. A Split Hopkinson Pressure Bar (SHPB) setup for three-point bending tests was used. Data of 20 tests were considered to be comprehensible for experimental characterization, thereby, showing an influence of strain rate on both time for fracture and amplitudes of force response. A three-dimensional porcine rib model was generated from the DICOM (Digital Imaging and Communication in Medicine) images of High-Resolution peripheral Quantitative Computed Tomography (HR-pQCT) scans. Material properties having been fitted by power law regression equations based on apparent density were assigned to the numerical rib. A modified elastic-plastic constitutive law, capable of considering the effects of strain rate was adopted. An incremental and stress-state dependent damage law, capable of considering effects of strain rate on fracture propagation, non-linear damage accumulation and instabilities was coupled to the constitutive law. The Finite Element (FE) model shows high efficiency in predicting both force-displacement curve and the fracture patterns of tested ribs. Predictions prove the ability of the proposed model to investigate the fracture behavior of human ribs under dynamic loads.

Keywords: Blunt Impact, Porcine Ribs, HR-pQCT, Finite Element Simulations, Fracture, Split Hopkinson Pressure Bar

[☆]Draft Manuscript, please do not cite without author's permission.

*Corresponding author

Email address: andre.langlet@univ-orleans.fr (André LANGLET)

1. Introduction

Rib fractures are frequent thoracic injuries, which are the principal causative factors in 30% of Road Traffic Accidents (RTA's) – Cavanaugh et al. (1993) – or High-Speed Ballistic Impacts (HSBI's), Shen et al. (2006). The human thorax contains vital and primary elements of respiratory and circulatory systems. The bone fragments originating from rib fracture may injure the heart, lung pleura, and lung parenchyma causing medical conditions like pneumothorax or hemothorax. This is why thoracic trauma is considered the second lethal trauma next to head trauma. In general, a chest trauma can be encountered either by Blunt thoracic trauma (BTT) or by Penetrating thoracic trauma (PTT), Arunan and Roodenburg (2017). The recent study on chest trauma by Fallouh et al. (2017) had reported that 98% of thoracic trauma is due to BTT. Burnside and McManus (2014) had presented a detailed summary on injury mechanisms and the severity of injury for BTT. Moreover, it is proved that RTA's are the principal cause for BTT and can be seen in Liman et al. (2003), Shirley (2005) and Horst et al. (2017). In fact, these mechanisms play an important role in the prediction of injury severity prior to radiological examination. Despite the existence of a concrete medical database, the mechanical behavior of ribs under impact loads is still vague. The knowledge of dynamic mechanical behavior and fracture patterns will aid us to understand the relationship between injury mechanism and the severity of the injury from Biomedical point of view.

The advances in computational ability and their advantages over expensive experimental procedures have led to the development of FE human body models such as Isolated thorax model (Schoell et al., 2015), the H-Model (Haug et al., 2004), the RADIOSS model (Arnoux et al., 2003), the THUMS model (Maeno and Hasegawa, 2001) and the HUMOS model (Robin, 2001). These FE human models have been used as a promising tool to overcome the limitations of experimental methods in the study of thoracic injuries. Even though these human FE models have advantages, they still have their respective constraints such as the representation of the structure, type of elements used and accuracy in prediction of fracture occurrence and mechanical behavior.

For a better comprehension of the dynamic behavior of ribs, the mechanical properties, numerical constitutive and damage laws should be addressed with equal priority. Regarding the mechanical properties, several authors have presented power law regression models. For example, Carter and Hayes (1977), Gibson (1985) and Keyak et al. (1994) have put forth power law regression equations with apparent density (ρ_{app}) as an independent variable as opposed to Rice et al.

(1988), who considered porosity (Po) or volume fraction (V_f) as independent variable. Apart from ρ_{app} based models, there are also models based on mineralization or ash fraction. For example, Vose and Kubala (1959) had considered ash fraction, whilst, Currey (1969), Burstein et al. (1975) and Schaffler and Burr (1988) had considered mineralization as independent variable.

Similar to elastic properties, significant amount of researches can be found on mechanical behavior. For example, cortical bone shows evidence of elastic-plastic behavior Garcia (2006) whilst, trabecular bone shows evidence of behavior similar to polymeric foams Gibson (1985), Kelly and McGarry (2012) and Karkar (2017). In fact, this difference in mechanical behavior is due to the architectural arrangement. Moreover, the bone material is strain rate ($\dot{\epsilon}$) sensitive as underlined by McElhaney (1966) and Carter and Hayes (1977). Thereby leading us to apply constitutive laws such as viscoelastic-viscoplastic (Johnson et al., 2010) and elastic-viscoplastic (Li et al., 2010). Zioupos et al. (2008) had shown that “*the strain rate has more effects on post-yield*” when the sample is subjected to high strain rates, thereby justifying the use of elasto-viscoplastic constitutive law in this study. Moreover, Zioupos et al. (2008) have also stated that “*micro-cracking is inversely proportional to strain rates*”, which justifies the use of a homogeneous model of the porcine rib in this study.

Numerous studies put forth concerning fracture criteria of bones have pointed out the limitations of basic fracture criteria models (e.g. von-Mises criteria, Hill’s criteria) to model the damage of bone. For example Malik et al. (2003), Taylor and Lee (2003), Vashishth et al. (2003), Ural and Vashishth (2007) and Abdel-Wahab and Silberschmidt (2011) had used fracture mechanics approach but failed to predict the complete fracture pattern, since these models are restricted to single dominant idealized planar crack. On the other hand, Hambli (2011a), Hambli (2011b) and Dall’Ara et al. (2013) have proposed damage models based on continuum damage mechanics (CDM). Most of these models are constrained to simulate bone fracture under monotonic load. There is a lack of practical FE models capable of simulating bone fracture under dynamic impact environment. The primary hurdle for simulating fracture in dynamic loads is to consider the effects of $\dot{\epsilon}$.

This study discusses the dynamic response of porcine ribs when subjected to three-point bending (3PB) upon split Hopkinson pressure bars (SHPB) apparatus. The SHPB method has proven to be particularly appropriate to characterize the behavior of quasi-brittle materials (e.g. Ruiz and Mines 1985) by applying a dynamic load to a specimen and to *calculate* both the impact

force and the velocity at the point of impact (input bar interface) and the reaction forces at the support (output bar interfaces).

The 3PB test is used to determine the tensile strength of quasi-brittle beam-like structures. In addition, the 3PB tests enable to analyze experimental measurements during the successive phases of the response, including the fracture phase. The dynamic response of the sample in the 3PB test depends on the relative order of magnitudes of the test duration (defined as time up to complete fracture) and the characteristic time of the structure. The response may be dynamic when its duration is comparable to the time taken by a wave for one to and fro motion from the point of impact to the sample extremities. This obliges to consider the transient motion of the sample. A spall response will be observed if the transit time through the specimen's transverse length and the test is of the same order as the the test duration. This has been pointed out by Delvare et al. (2010). In the present experiments, the rib responses were identified either in the dynamic response or in the spall response.

An elastoviscoplastic constitutive model coupled with an external damage law, which considers the effects of $\dot{\epsilon}$ on behavior and fracture of rib, has been implemented on a FE model of the porcine rib.

The FE model shows high efficiency in predicting both the force-displacement curve and the fracture patterns of tested ribs.

2. Experimental Methods

2.1. *Dynamic three-point bending tests*

Fresh porcine ribs were subjected to dynamic 3PB tests. The muscles and tissues surrounding the ribs were removed prior to tests.

The experimental set-up consists of three bars: the input bar (3 m long) and two output bars (1.75 m). The rib sample is simply supported between the three bars as shown in Fig. 1. The rib extremities were sanded to a plane surface so that a stable and homogeneous contact is established with each output bar at the two output interfaces, Fig. 2.

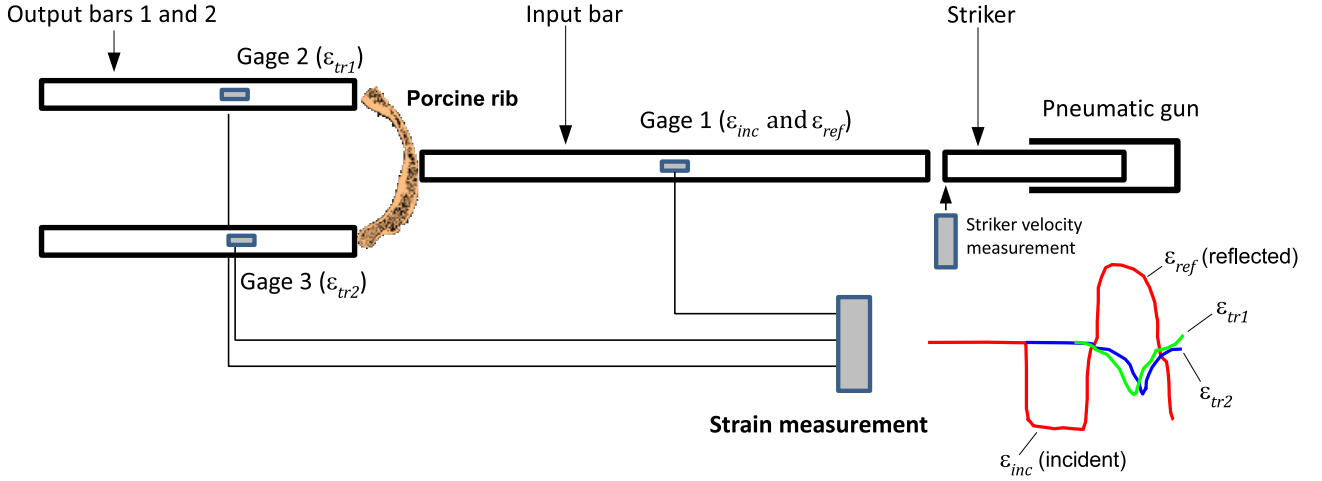


Figure 1: SHPB apparatus for bending tests

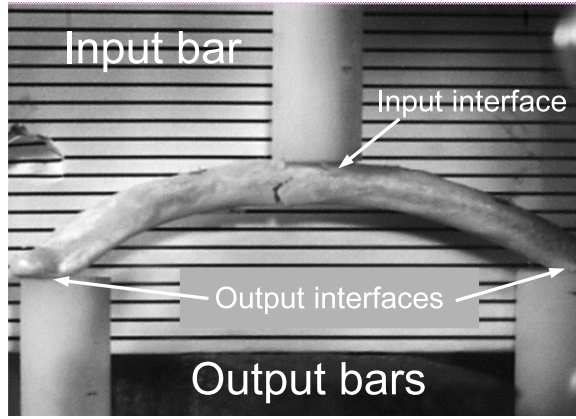


Figure 2: The rib sample placed in between the bars with a visible fracture

The signal acquisition frequency in the set up is 1 MHz. Strain gages were placed at the mid-point of input bar and at 400 mm from the output bar-sample interface on output bars to obtain strain signals for post-processing.

The principle of the test is to generate a compressive pulse wave which is created by the striker impacting the input bar. The duration of this wave is the time taken for one to and fro motion along the striker. As the wave arrives at the rib-bar interface, a part of it is reflected and the other part is transmitted to the output bars. Processing of the data required the strain histories measured on the three bars by three strain gages. The absolute time origin, $t' = 0$, is defined by the optical velocity measurement device when the sriker passes a LASER beam, thereby triggering the measurement chain. On the input bar, the first gage measures the incident and reflected longitudinal normal strains *vs.* time t' : $\varepsilon_{inc}(t')$ and $\varepsilon_{ref}(t')$, respectively. On each output bar, the

second and third gages measure the transmitted strains $\varepsilon_{tr1}(t')$ and $\varepsilon_{tr2}(t')$.

A time and space shifting procedure is applied in data processing. It consists of defining an origin t'_0 which coincides with the arrival time of the incident wave at the input bar-sample interface:

$$t = t' - t'_0 \quad (1)$$

All of the strains are then related to the relative time, as if they were measured at the bar-sample interfaces (this procedure is known as the “time and space” shifting of the strain waves).

In case of stress below yield limit of the bar material, application of formula describing the plane wave propagation would lead to the dynamic variables at the input and output bar-sample interfaces (subscripts “*inp*” and “*out1*”, “*out2*” respectively): the reaction forces F , the interface velocity and displacement v , u :

$$F_{inp} = A_B E_B [\varepsilon_{inc}(t) + \varepsilon_{ref}(t)] \quad (2a)$$

$$F_{out1} = A_B E_B \varepsilon_{tr1}(t) \quad (2b)$$

$$F_{out2} = A_B E_B \varepsilon_{tr2}(t) \quad (2c)$$

$$v_{inp} = -c_B [\varepsilon_{inc}(t) - \varepsilon_{ref}(t)] \quad u_{inp} = \int_0^t v_{inp} dt \quad (2d)$$

$$v_{out1} = -c_B \varepsilon_{tr1}(t) \quad u_{out1} = \int_0^t v_{out1} dt \quad (2e)$$

$$v_{out2} = -c_B \varepsilon_{tr2}(t) \quad u_{out2} = \int_0^t v_{out2} dt \quad (2f)$$

where E_B , ρ_B , and A_B , are the bar Young modulus, mass density, and cross-sectional area respectively and the celerity of longitudinal waves is $c_B = \sqrt{E_B/\rho_B}$.

The relative velocity V and displacement U of the input bar-sample interface are defined by:

$$V = v_{inp} - \frac{(v_{out1} + v_{out2})}{2} \quad (3)$$

$$U = \int_0^t V dt \quad (4)$$

Since the mechanical impedance of rib (the mass density times the acoustic wave velocity in the material) is considerably lower than that of usual metallic bars, such classical bars cannot be

used for this study as the impedance ratio would lead to a nearly zero transmission coefficient and a reflection coefficient close to 1. Thereby leading to a weak reaction force at the input bar - sample interface, as if the interface was a free interface. Hence, bars made of nylon were used in the present study.

The strains measured at the remote gage locations must be corrected to yield the signals at the interfaces. Several authors, among which Zhao and Gary (1995), Zhao et al. (1997), proposed a visco-elastic correction based on the Pochhammer-Chree model in infinite cylinders. The dispersion equation was solved and provided a correction that takes both dispersion and damping into account. In the present work, the shifting procedure is carried out by the DAVID software (Gary, 2005) built under the LABVIEW[®] environment. The DAVID interface is used to calculate the dynamic forces F_{inp} , F_{out1} , F_{out2} from the strain signals.

The second question to be addressed is non-plane wave effect, due to the possibility of non-uniform strain distribution over the normal cross-section of the bar. On the external bar surface, the strain can even be zero while being non-zero within the cross-section. This issue of great importance has been discussed by Merle and Zhao (2006) considering the bar radius and the spectrum of the pulse wave and the material (steel, aluminum, nylon). For the experimental conditions of the present study, the assumption of uniform strain distributions (plane waves) leads to a maximum errors less than 5% (Merle and Zhao, 2006). Therefore, the correction applied to measured strains was only for the dispersion, but not for three dimensional effects.

The application of the use of nylon bars for dynamic three-point bending tests on ribs can be seen in Aubert et al. (2012).

A mirror and a high-speed camera was placed on either side of the rib to record the test at an acquisition frequency ranging from 11000 images/s to 25000 images/s until rupture of the specimen.

2.2. Rib geometrical model and elastic properties

A batch of porcine ribs was bought from a local meat processing plant in order to ensure homogeneity of samples. These ribs were stored in a cloth soaked in saline (9% NaCl) to avoid dehydration and stored in a refrigerator at 4° C whilst not in use. They were defatted in an aqueous solution of sodium hypochlorite (NaClO) and salt (NaCl) prior to the computed tomography (CT) scan. Later, they were scanned using High-Resolution peripheral Quantitative Computed Tomography (XtremeCT, Scanco, Switzerland). The DICOM image slices were obtained using a

multi slice device at 120 kVp, 160 mAs with a 512×512 image matrix and 150×150 mm field view. Each image slice was 7 mm thick with a spatial resolution of $0.25 \text{ mm} \times 25 \text{ mm}$ as in Fig. 3.

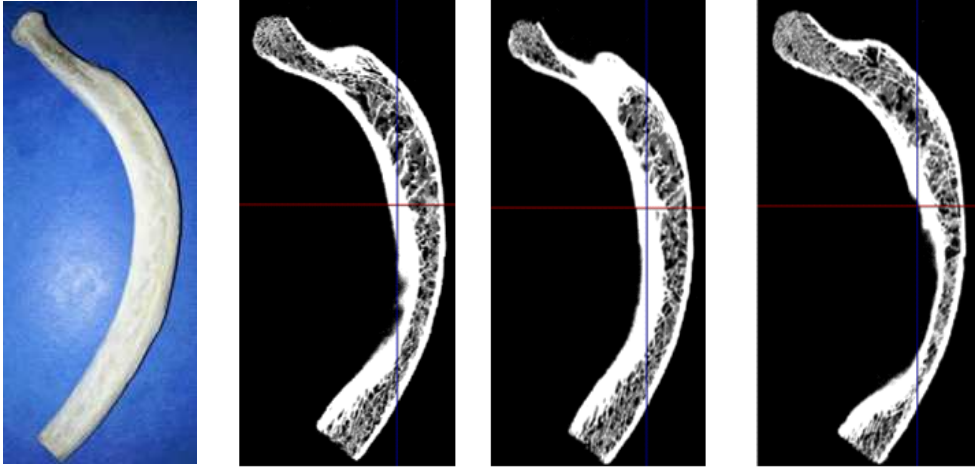


Figure 3: Treated porcine rib and CT scan images

A 3D geometry was then created from the contours of the DICOM images in order to generate a hexahedral mesh for numerical simulations. ScanIP module of Simpleware[®] code Trial version, (Simpleware[®], 2014), was used to import the DICOM raw data, perform image processing, visualization and segmentation of the rib geometry. A distribution of 8 grey scale intensities (see Tab. 1) was chosen to determine the heterogeneous mechanical properties of eight parts within the rib. A grey intensity (or level) is associated with a particular value of the linear attenuation coefficient μ . Five-sample calibration phantom (Mindways[®]) with known equivalent K_2HPO_4 and H_2O densities was placed below the rib during the scan. Using an algorithm implemented into Simpleware[®] code, we obtained the linear calibration coefficients μ to convert the raw data into normalized data (GS), expressed in Hounsfield Units (HU) using the following linear expression (Taylor et al. 2002, Teo et al. 2006):

$$GS = 1000 \frac{(\mu_b - \mu_w)}{(\mu_w - \mu_a)}; \mu_w = 0; \mu_a = -1000. \quad (5)$$

where: μ_b , μ_w , and μ_a are the values for bone, water and air respectively. This was done by calculating the average GS within each of the five calibration samples along the length of the scan and calculating the slope and intercept *vs.* the known equivalent K_2HPO_4 and H_2O densities.

According to Taylor et al. (2002), GS is related to the effective density ρ_{eff} (which includes the masses of: bone, bone marrow and fluids), whereas ρ_{app} excludes the bone marrow.

Effective density ρ_{eff} (Fig. 4) is defined as:

$$\rho_{eff} = 0.523 GS + 1000 \quad (6)$$

Apparent density ρ_{app} is calculated using a linear relationship with zero intercept (see Fig. 4):

$$\rho_{app} = 1.2097 GS \quad (7)$$

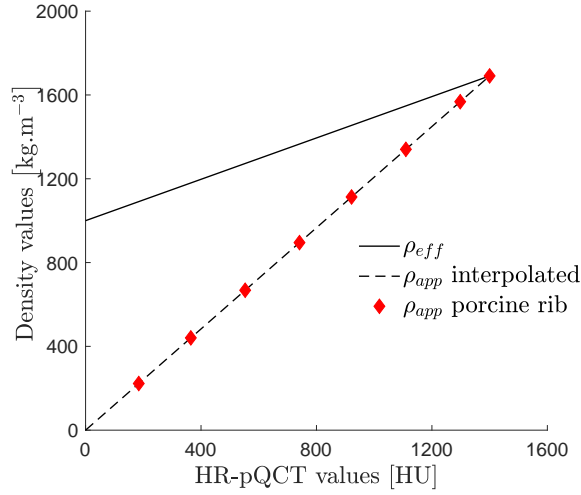


Figure 4: Effective and apparent density with respect to GS value.

To distinguish the different constituents of porcine rib, we had used the porosity (PO) calculated from volume fraction V_f .

$$PO = 1 - V_f = 1 - \frac{\rho_{app}}{\rho_{tissue}} \quad (8)$$

where, $\rho_{tissue} = 1850 \text{ kg/m}^3$ is the density of the solid bone tissue. As we assume that both cortical bone and trabecular bone are of similar composition, the tissue density was considered same for porosity calculation. The grey scales, the porosity values and standard deviation of the eight parts are given in Tab.1. The standard deviation was estimated through the resolution of the imaging system.

Part number	Greyscale intensity	Porosity	S. dev. (%)
1	184.314	87.96%	1.541
2	364.706	76.18%	3.139
3	552.941	63.90%	4.408
4	741.176	51.61%	6.113
5	921.569	39.83%	7.780
6	1109.800	27.54%	9.256
7	1298.040	15.25%	10.840
8	1400.000	8.60%	11.167

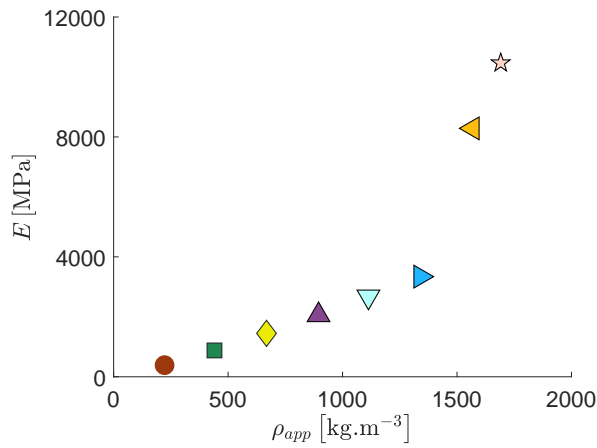
Table 1: Grey scale values for porcine rib in Hounsfield Units HU and corresponding standard deviation (S. dev.)

Based on the porosity, respective power law regression equations were used to obtain the mechanical properties (see Tab. 2). The equations for cortical bone and trabecular bone were adapted from Doblaré et al. (2004) and Kopperdahl and Keaveny (1998) respectively.

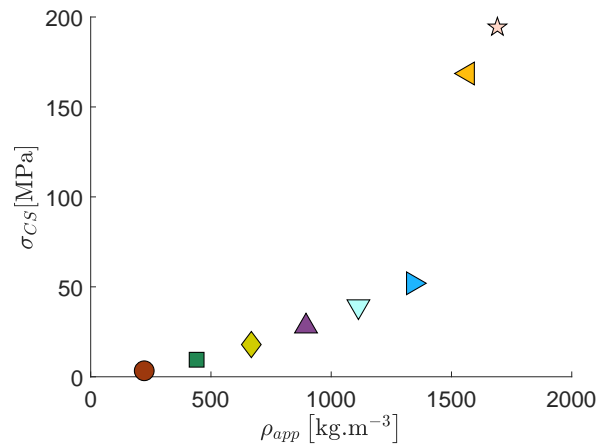
Property	Cortical	S. dev. (%)	Trabecular	S. dev. (%)
Young's Modulus E	$1.109 \times 10^{-6} \rho_{app}^{3.09}$	23.33	$0.5903 \rho_{app}^{1.20}$	24.20
Compressive Strength σ_{uC}	$1.659 \times 10^{-4} \rho_{app}^{1.88}$	15.46	$8.534 \times 10^{-4} \rho_{app}^{1.53}$	21.45
Tensile Strength σ_{uT}	$1.61 \times 10^{-4} \rho_{app}^{1.88}$	12.32	$8.201 \times 10^{-4} \rho_{app}^{1.07}$	21.74
Compressive Yield σ_{yC}	$1.422 \times 10^{-4} \rho_{app}^{1.85}$	19.76	$5.167 \times 10^{-4} \rho_{app}^{1.60}$	24.58
Tensile Yield σ_{yT}	$3.064 \times 10^{-4} \rho_{app}^{1.67}$	18.45	$7.5686 \times 10^{-3} \rho_{app}^{1.04}$	26.85

Table 2: Power law regression equations used for mechanical properties (unit for stresses is here MPa) and standard deviation estimations based on the power laws and of the standard deviation of the grey scale intensity

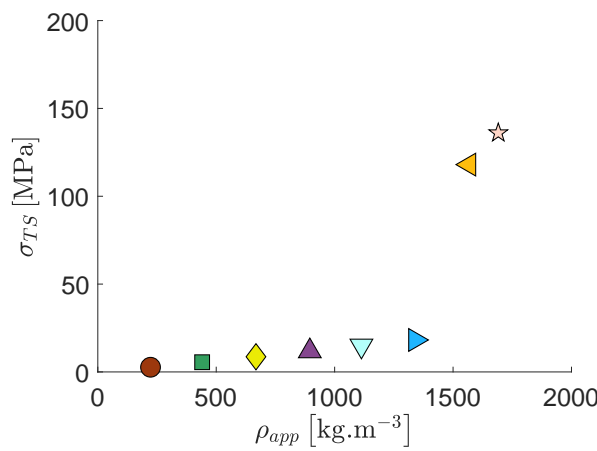
The mechanical properties of the constituents in terms of ρ_{app} are plotted in Fig. 5 (the standard deviations are given in Tab. 1). Among the properties listed in Tab. 2 the following will intervene in material model of the rib: apparent density ρ_{app} , Young Modulus E , and tensile yield stress σ_{yT} .



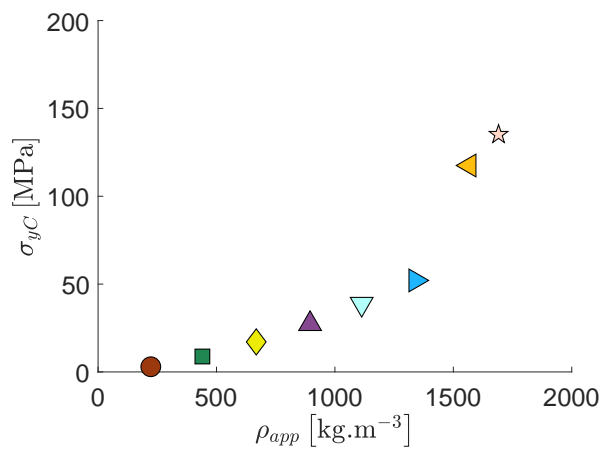
(a) E vs. ρ_{app}



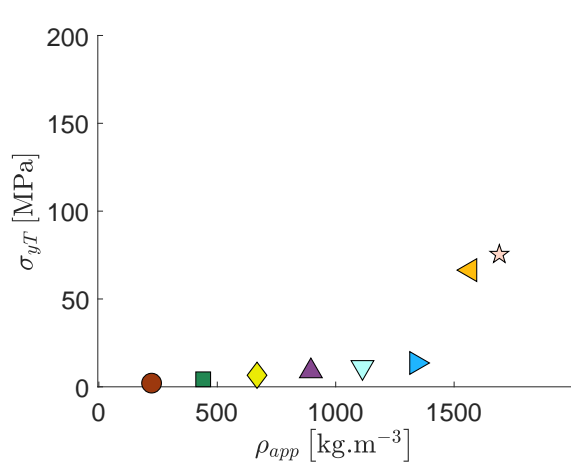
(b) σ_{CS} vs. ρ_{app}



(c) σ_{TS} vs. ρ_{app}



(d) σ_{yC} vs. ρ_{app}



(e) σ_{yT} vs. ρ_{app}

	Po [%]	ρ_{app} [kg/m ³]	
●	87.97	222.61	(Tr)
■	76.19	440.48	(Tr)
◆	63.90	667.83	(Tr)
▲	56.61	895.81	(Tr)
▼	39.83	1113.81	(Tr)
▶	27.54	1340.40	(Tr)
◀	15.26	1567.80	(Co)
☆	8.60	1690.90	(Co)

Figure 5: Mechanical properties for constituents of porcine rib for different porosities or mass densities. Co: Cortical bone, Tr: Trabecular bone

3. Material models

3.1. Striker and Bars

As the nylon bars and striker are weakly viscoelastic, damping and dispersion of the waves during the first to and fro motion along the bars are moderate. Therefore, an elastic constitutive law is assumed for the bars and striker in numerical model. In the present case, this hypothesis does not fundamentally affect the simulation results as it will be justified later.

The material properties of bars and striker were determined through longitudinal wave celerity obtained after an impact of the striker on the free input bar. Knowing the mass density $\rho_B = 1200 \text{ kg.m}^{-3}$, the Young modulus E_B was found to be 3.3 GPa. The Poisson's ratio 0.4 was determined from transverse and longitudinal strain measurements

3.2. Rib

3.2.1. Constitutive law

The classic elastic-plastic law was modified to consider the effects of strain rate $\dot{\epsilon}$. Zioupos et al. (2008) and Li et al. (2010) have shown that the effect of strain-rate is of much less importance in the elastic regime. Therefore, in the present work, the strain-rate effect is taken into consideration only in post-yield regime. This could be achieved by two ways: (i) by providing stress-strain curves defined at various $\dot{\epsilon}$; (ii) by scaling the dynamic yield stress with respect to $\dot{\epsilon}$. The second way is based on *Cowper-Symmonds* model, expressed as:

$$\frac{\sigma_{yd}}{\sigma_{y0}} = 1 + \left(\frac{\dot{\epsilon}}{C} \right)^{1/P} \quad (9)$$

where, σ_{yd} is the dynamic yield stress, C and P are Cowper-Symmonds parameters. The initial yield stress σ_{y0} is identified as σ_{yT} given in Tab. 2. The values of C and P were taken from Li et al. (2010): $C = 2.5 \text{ GPa}$, $P = 7$.

The cortical and the trabecular bones were modeled using elastoviscoplastic behavior.

Cortical and trabecular bones were supposed to obey isotropic and kinematic hardening respectively, as it was demonstrated by previous studies: Garcia (2006) and Wolfram and Jakob (2016) for cortical, Keaveny et al. (1999) and Li et al. (2010) for trabecular.

3.2.2. Damage law

Even though the material models offer element deletion based on fracture strain ϵ_f , it is not sufficient to capture the evolution of crack and damage initiation whilst the bone is subjected to

Curve number	$\varepsilon_{fd}/\varepsilon_{fs}$
1	$0.63 - 1.00 \times 10^{-2} \text{Ln } \dot{\varepsilon}$
2	$0.63 - 1.25 \times 10^{-2} \text{Ln } \dot{\varepsilon}$
3	$0.63 - 1.60 \times 10^{-2} \text{Ln } \dot{\varepsilon}$
4	$0.63 - 2.00 \times 10^{-2} \text{Ln } \dot{\varepsilon}$
5	$0.63 - 4.00 \times 10^{-2} \text{Ln } \dot{\varepsilon}$

Table 3: List of different $\varepsilon_{fd}/\varepsilon_{fs}$ vs. $\dot{\varepsilon}$ relations tested (plotted Fig. 6b)

impact.

Thus, the constitutive law was coupled to an incremental and stress-state dependent damage law which also considers damage accumulation, (ΔD), Frieder et al. (2009), Fillipe et al. (2014).

The triaxiality is defined as:

$$\eta = -\frac{-\frac{1}{3}\text{tr } \boldsymbol{\sigma}}{\sigma_{eq}} \quad (10)$$

where: $\frac{1}{3}\text{tr } \boldsymbol{\sigma}$ is the hydrostatic pressure (average of the $\boldsymbol{\sigma}$ stress tensor trace) and σ_{eq} is the equivalent stress.

The relation between the fracture strain ε_{fd} and triaxiality η – Eq. (10) – is given in the form of an input curve plotted in Fig. 6a.

In this study, the static fracture strain ε_{fs} value is 2×10^{-2} m/m for cortical and 3×10^{-2} m/m for trabecular bone. To approach the realistic fracture and propagation behavior using our damage model, the influence of strain rate $\dot{\varepsilon}$ on the fracture strain ε_{fd} was implemented by an equation from Wood (1971) as follows:

$$\frac{\varepsilon_{fd}}{\varepsilon_{fs}} = A - B \text{Ln } \dot{\varepsilon} \quad (11)$$

where $A = 0.63$. Five different values of B were tested. The corresponding expressions of Eq. (11) are listed in Tab. 3 and the input curves for $\varepsilon_{fd}/\varepsilon_{fs}$ vs. $\dot{\varepsilon}$ are plotted in Fig. 6b.

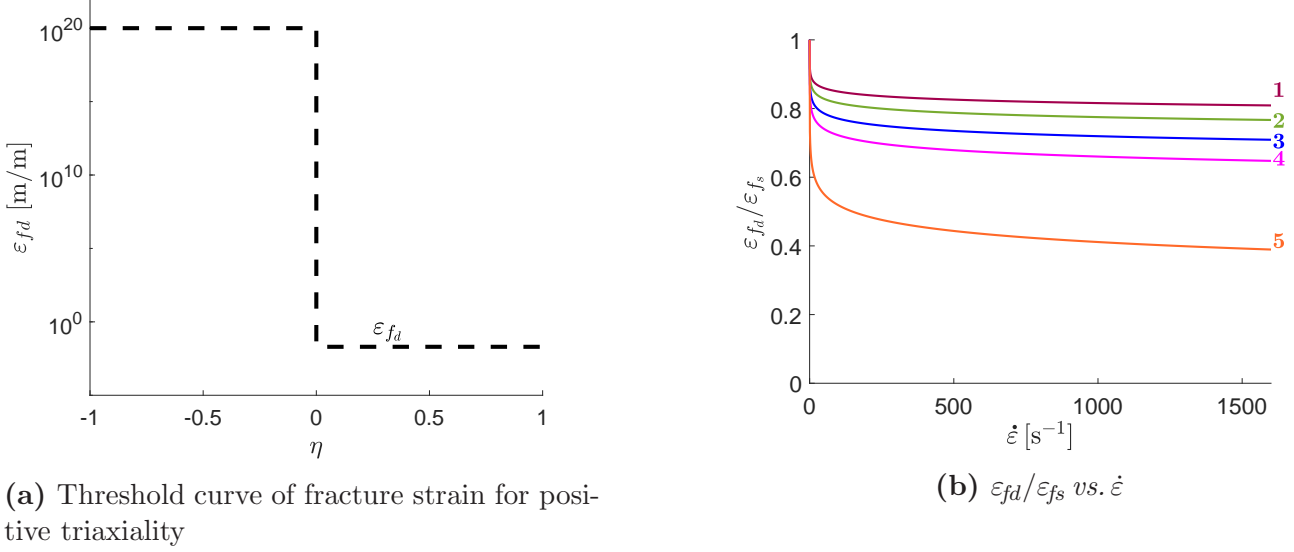


Figure 6: Input curves of damage law

Note that the static fracture strain provided by Wood (1971) is 0.86×10^{-2} m/m, which corresponds to a quasi-static strain-rate of 3.18×10^{-3} s⁻¹. Similarly, in the present study Eq. (11) is not applicable for $\dot{\varepsilon}$ lower than 3.00×10^{-3} s⁻¹, which are quasi static. For all values $0 \text{ s}^{-1} \leq \dot{\varepsilon} \leq 3.00 \times 10^{-3} \text{ s}^{-1}$, a linear approximation is applied so that $\varepsilon_{fd}/\varepsilon_{fs} = 1$ at $\dot{\varepsilon} = 0 \text{ s}^{-1}$.

The increments in damage ΔD is expressed in terms of plastic strain $\Delta\varepsilon_p$, triaxiality η and $\dot{\varepsilon}$ as follows:

$$\Delta D = \frac{n}{\varepsilon_{fd}(\eta, \dot{\varepsilon})} D^{(1-1/n)} \Delta\varepsilon_p \quad (12)$$

The damage exponent n is to differentiate between linear and non-linear damage accumulation.

The reduction in load carrying capacity due to increase of damage is taken into account through a modified equation of Lemaitre's effective stress principle:

$$\boldsymbol{\sigma} = \tilde{\boldsymbol{\sigma}} (1 - D^m) \quad (13)$$

where $\tilde{\boldsymbol{\sigma}}$ is the effective stress tensor.

When the damage D reaches 1.0, fracture occurs and the gaussian integral point of the corresponding element no longer exists in the calculation.

The parameters used for damage law are given in Tab 4. The damage exponent n values were adapted from Wolfram et al. (2011). Unfortunately, the lack of database on the fading exponent m for bone had led us to use $m = 1.0$.

When the yield stress is reached damage D starts to accumulate according to Eq. (12). The fracture strain ε_{fd} influences this accumulation. The more ε_{fd} decreases with increasing strain-rate, more drastic will be the increase in damage accumulation ΔD and in $\Delta\varepsilon_p$.

The ultimate damage value $D = 1$ is reached through the non-linear coupling between damage D , fracture strain $\varepsilon_{fd}(\eta, \dot{\varepsilon})$, plastic strain ε_p and softening. When $D = 1$, the corresponding element is removed from the structure, thereby initiating the crack propagation until fracture.

The strain rate influence on the post-yield behavior is also clear on the energy W absorbed by the structure. The more rapid is ε_{fd} decreases with respect to $\dot{\varepsilon}$, the less is the energy absorbed.

3.3. Average properties of rib

The constitutive law of cortical and trabecular bone of porcine rib could be recapitulated through mean values of the elastic properties. These values are summarized in Tab. 4 and the damage law parameters as well.

Law	Parameter [units]	cortical bone	trabecular bone
Constitutive	ρ_{app} [kg.m ⁻³]	1690.90	772.90
	E [GPa]	9.374	1.80
	ν	0.3	0.45
	$\sigma_{y0} = \sigma_{yT}$ [MPa]	70.876	20.48
	E_{TAN} [GPa]	0.937	0.0450
	C [GPa]	2.5	2.5
	P	7.0	7.0
Damage	n	1.2	2.0
	m	1.0	1.0
	ε_{fs} [m/m]	2.0×10^{-2}	3.0×10^{-2}

Table 4: Average properties of rib and parameters used in numerical calculation

It is remarkable that the values presented here are the same order of magnitude to that of human ribs published by Charpail (2006), Li et al. (2010) and Yates and Untaroiu (2018).

4. Finite element model

The simulations were executed with LS-DYNA[®] explicit solver (Livermore, LSTC[®], CA).

4.1. Mesh and Boundary Conditions

4.1.1. Mesh

The SHPB bars were meshed with solid hexahedral elements. For an accurate simulation of 1D longitudinal wave propagation in bars, the element length in the direction of propagation was

considered to be 1 mm.

In the case of ribs, the 3D geometry generated through DICOM images was meshed with hexahedral elements using Simpleware[®] ScanIP (Synopsys[®], CA) Fig. 7. Previous studies that investigated the model convergence recommended using an element of size less than 3 mm to accurately capture the heterogeneous variations in the mechanical properties (Keyak et al. 1994, Bessho et al. 2007) and to ensure an accurate prediction of the fracture path growth (Hambli, 2013). Therefore, an element size of about 0.15 mm was retained to mesh the ribs leading to a total of 226520 eight nodes hexahedral (solid brick) elements. For the sake of optimization of calculation time, bar and rib elements were assigned one Gaussian integral point only. To avoid volumetric locking or Hourglass modes, a Flanagan-Belytschko stiffness form (Flanagan and Belytschko, 1981) with an exact volume integration Hourglass formulation was selected. In fact, to avoid instabilities in solid elements, the Hourglass coefficient for bars was set to 0.03 whilst, the Hourglass coefficient for bone elements was set as default (0.1).

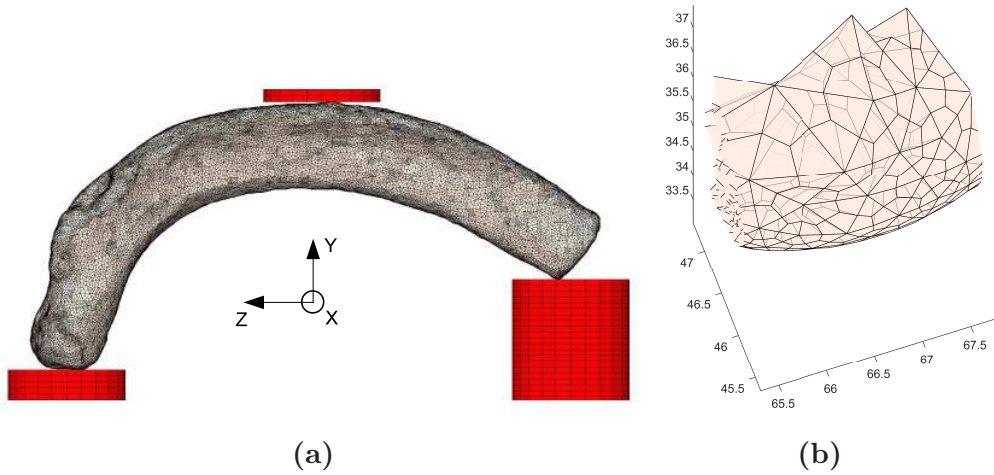


Figure 7: Finite element mesh of porcine rib and bars (a) and zoom of the left rib extremity showing the hexahedral elements (b) – dimensions in mm

The trabecular and cortical properties presented in the subsection 2.2 were assigned through their spatial localization provided by the CT scan images. The resulting density (ρ_{app}) distribution is presented in Fig. 8, showing the imbrication of parts of differing properties.

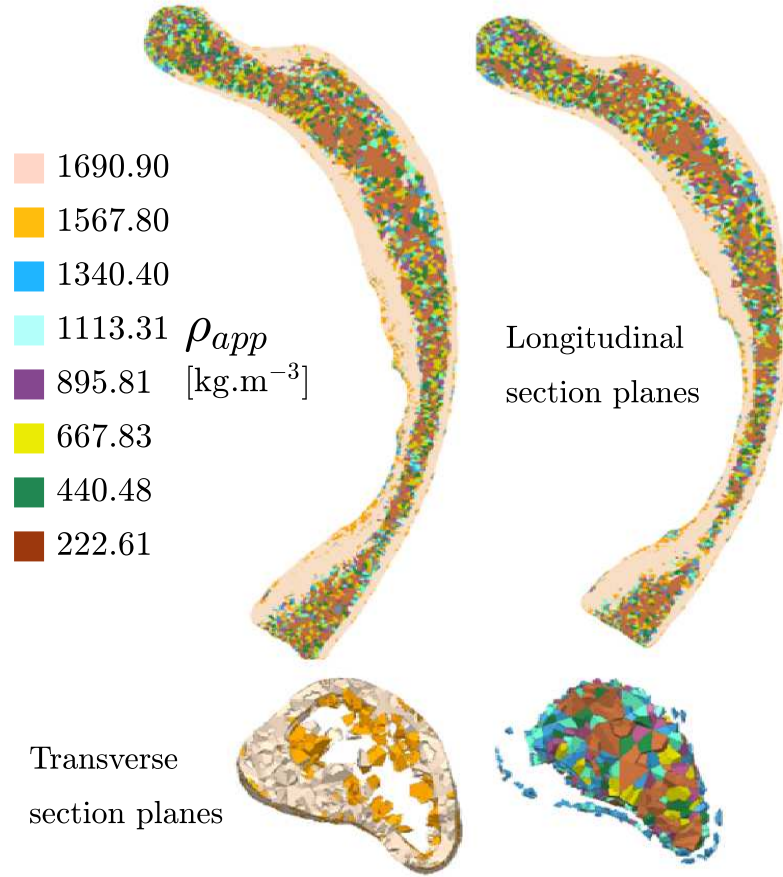


Figure 8: Cross-sectional views of the rib FE model showing the density distribution (color code is the same as in Fig. 5).

4.1.2. Boundary Conditions

The nodes belonging to rib were left free *i.e.* no constraints in motion. However, they may be subjected to reaction forces at the contact interfaces. This is also applicable at the input bar and striker contact interface.

The nodes belonging to striker were assigned an user defined initial velocity, in this case, $v_{striker} = 17.39 \text{ m}\cdot\text{s}^{-1}$, which corresponds to the selected experimental test to be modeled. For this case, fracture occurs before the dynamic equilibrium is established.

4.2. Contact

A penalty based “*Surface-to-Surface Contact*” algorithm was defined between the sample and bars. The friction coefficient is 0.1. A segment-based approach was invoked, which searches for penetration of master and slave segments and then applies the penalty force on segment nodes instead of searching the penetrating nodes and then applying the forces to segments. In addition to

this, the segment based approach stores the initial penetration value of segments and removes them from the current penetration value before calculating the contact force, thereby avoiding node-shoot-out if a large penalty force is detected. Thanks to the contact formulation, the interface forces can be extracted from the contact data thereby providing us a criterion to compare the numerical and experimental structural response.

Another contact algorithm (“*Contact-Interior*”) is defined between each constituent (visible in Fig. 8) in order to represent the internal cohesion of the structure. By doing so, the solver is capable to apprehend that these constituents form a single structure.

5. Experimental Results

5.1. Analysis of force response

A total of 20 tests were considered to be worthy for analyzing the experimental response. The results can be distinguished into two categories: (1) tests with no fracture, (2) tests with fracture.

(1) **Tests with no fracture.** We observe three different phases in the force response. **Phase A:** during this short phase (*till* $300 \times 10^{-6}s$), there is a brutal increase in input force whilst, the output force is still zero. The sample is in an out-of-equilibrium state. Phase A will be observed in any experimental test. **Phase B:** the rib is subjected to forces applied by the two output bars (*between* $300 \times 10^{-6}s$ and $700 \times 10^{-6}s$). The input force F_{inp} and the resultant $\Sigma F_{out} = F_{out1} + F_{out2}$ are almost equal meanwhile showing evidence of small oscillations. **Phase C:** a dynamic equilibrium is established between F_{inp} and ΣF_{out} which occurs beyond $700 \times 10^{-6}s$, and the oscillations disappear. As no fracture occurred, the brutal decrease (similar to a discontinuity) in the contact force signals is not observed (Fig. 9a).

(2) **Tests with fracture.**

(a) During dynamic equilibrium phase: Similar to tests with no fracture, a brutal increase in F_{inp} is observed, followed by a plateau phase. A dynamic equilibrium is established around $600 \times 10^{-6}s$ (see Fig. 9c) in this case. The important characteristic in this kind of response is that the crack propagation and fracture occur during the equilibrium phase. The fracture of the rib corresponds to the rapid fall in force signals.

- (b) During the non-equilibrium phase: Fig. 9e shows respective characteristics of fracture during the non-equilibrium phase. The sample has no time to establish an equilibrium between F_{inp} and ΣF_{out} . The fracture of rib occurs around 500×10^{-6} s, way before the equilibrium is established.

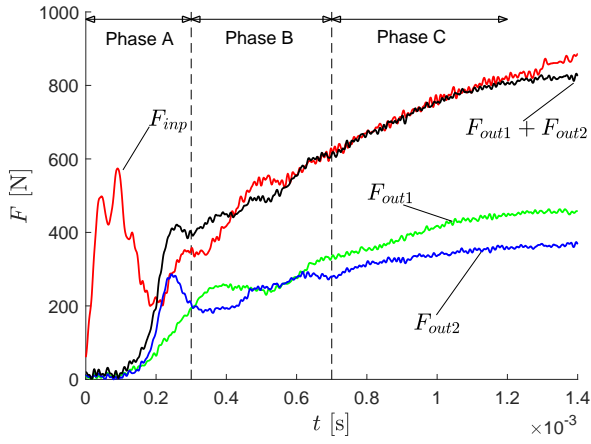
5.2. Structural response of rib and corridors

The structural response was studied through the force-displacement curve F_{inp} vs. U . The interface relative velocity V and relative displacement U between the surface of bars and the rib are calculated through Eqs. (3), (4), respectively.

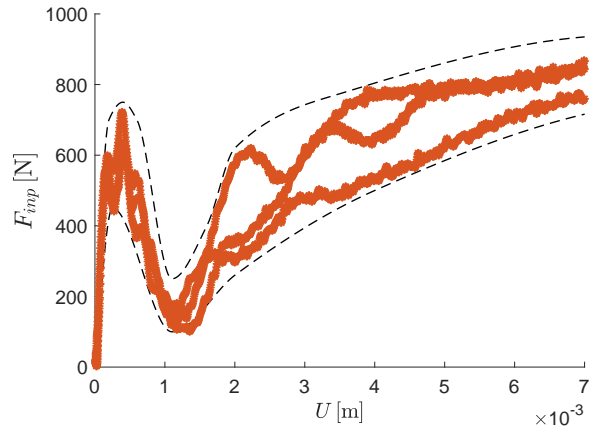
Three categories of structural responses are distinguished according to the interface velocity V . Maxima and minima of the ensemble of each category define the experimental corridors 1, 2 and 3.

- (1) $5 \leq V \leq 7$ m/s, Fig. 9b.
- (2) $8 \leq V \leq 10$ m/s, Fig. 9d.
- (3) $11 \leq V \leq 13$ m/s, Fig. 9f.

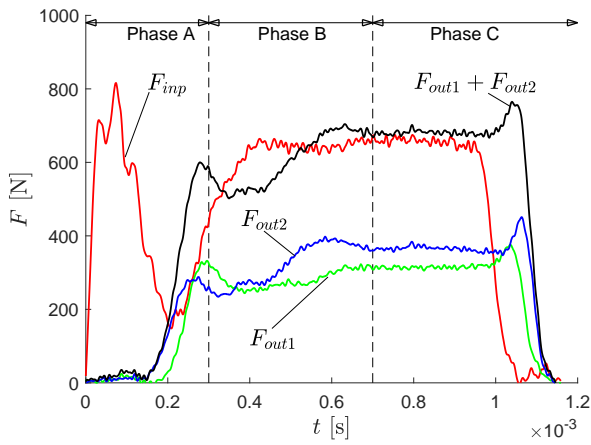
Through these experimental corridors, we notice that as the velocity V increases, the fracture of rib tends to occur at dynamic non-equilibrium phase.



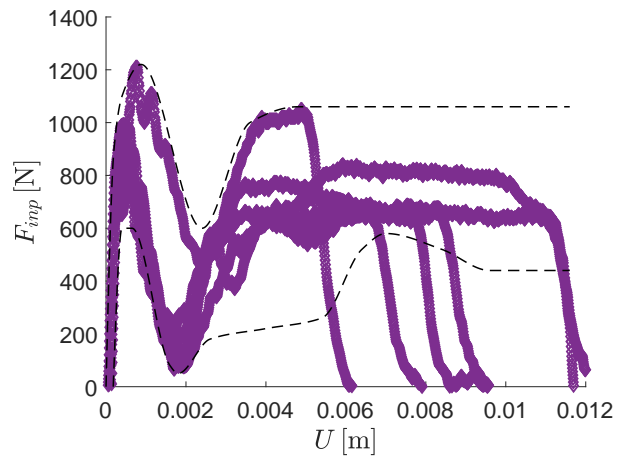
(a) F_{inp} and F_{out} vs. t for no fracture



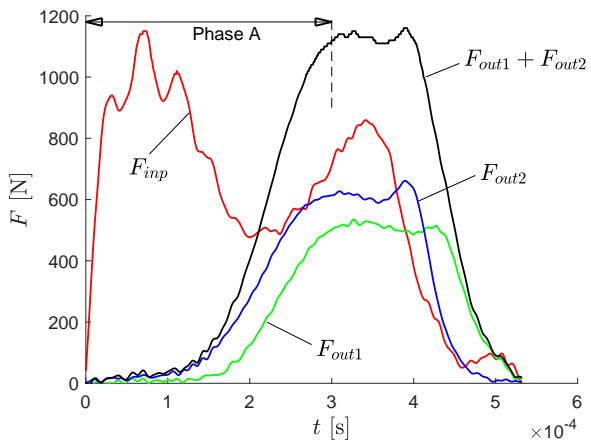
(b) Experimental Corridor-1



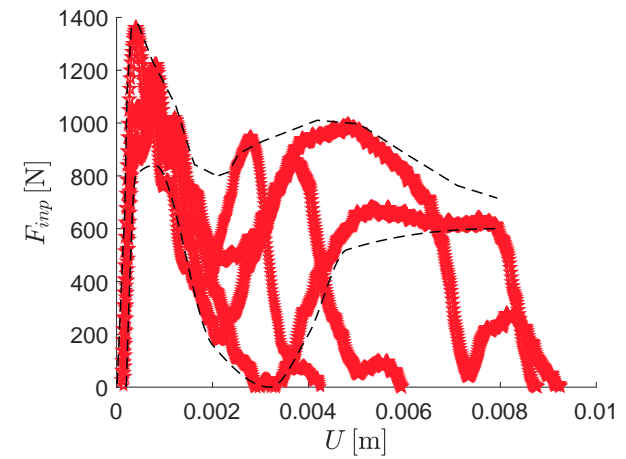
(c) F_{inp} and F_{out} vs. t for fracture in equilibrium



(d) Experimental Corridor-2



(e) F_{inp} and F_{out} vs. t for fracture before equilibrium



(f) Experimental Corridor-3

Figure 9: Experiment Results

6. Numerical results and validation of the model

6.1. About the constitutive and damage laws

The FE model is capable of deleting element thereby resulting in “erosion” of the structure. For tensile stresses or strains, elements can be deleted *either* when $D = 1$, *and/or* the strain reaches the dynamic fracture strain ε_{fd} . For compressive stresses, element deletion is not allowed by the triaxiality criterion (Fig. 6a) but may occur only when damage D reaches the unit value in an element.

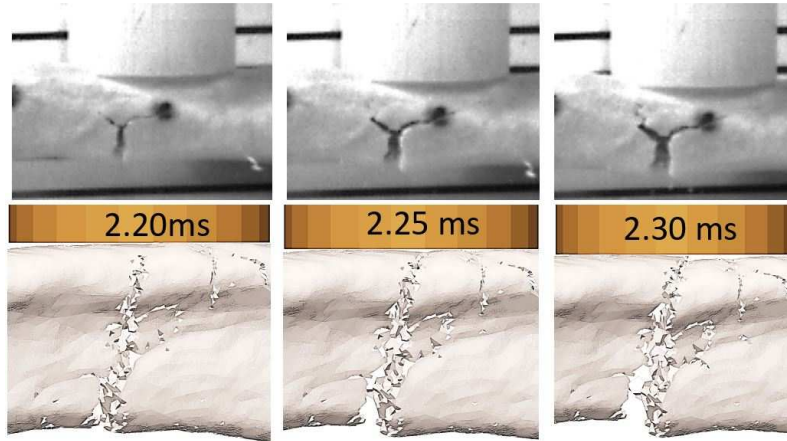


Figure 10: Comparison of experimental (top) and numerical fracture pattern (bottom) at different t' times values

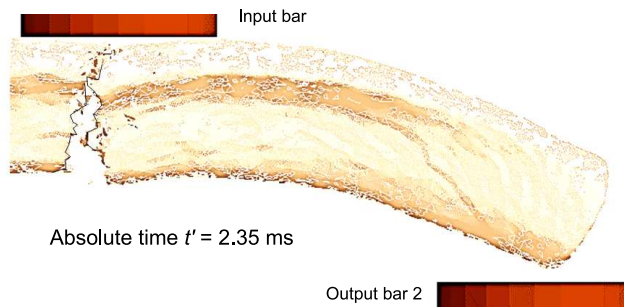


Figure 11: Loss of contact between rib and output bar 2 after fracture (simulation)

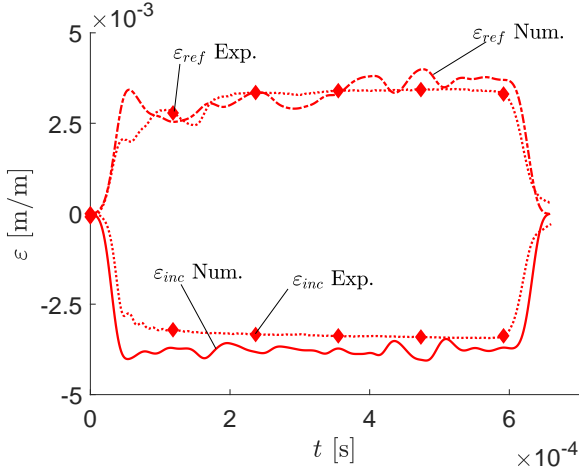
Therefore, the fracture propagation being simulated is essentially governed by the tensile behavior of the FE model, but, also slightly influenced by the damage caused by compressive stresses. Note that the response mode of the rib is similar to a bending mode. Then, the compression and tension zones are in general symmetrically localized about the cross-section centroid. In such case, erosion of a few elements by compression may accelerate the onset of fracture in tension.

For this reason, the tensile yield stress σ_{yT} has been assigned to the yield stress σ_{y0} in the material model definition (section 3).

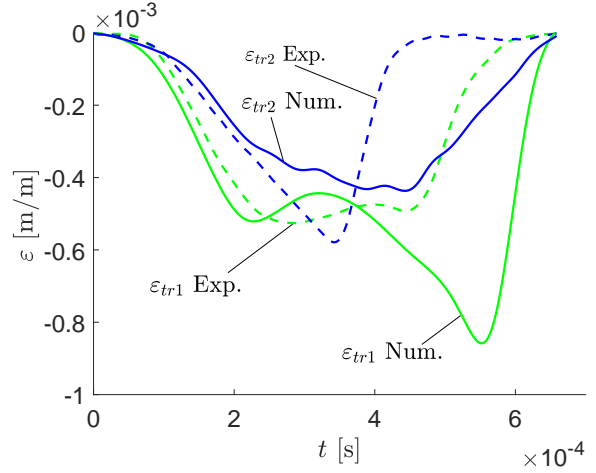
The fracture pattern can be observed in Fig. 10. It is evident that the crack starts to propagate from the surface subjected to tension towards the point of impact and is a purely local phenomenon. It appears that the crack originates at the same point. Other common characteristics shared between experimental and numerical fracture patterns are the Mode-I crack and the time interval in both cases is 0.13×10^{-3} s.

6.2. Consistency of the numerical strain, velocity and displacements time histories

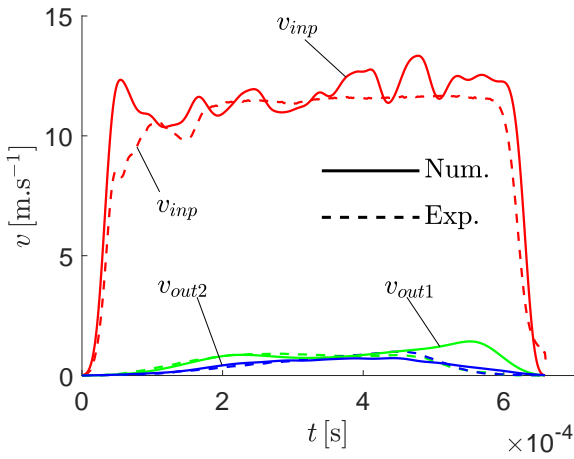
To verify the pertinence of the FE model, the first stage is to validate the numerical time histories of strain at the interfaces. In effect, every physical quantity inferred from the SHPB tests are based on the interface strains. Therefore, it is mandatory to verify the relevancy of the numerical interface strains with the experimental results. Moreover, the relevancy of the velocity and displacement histories must also be verified.



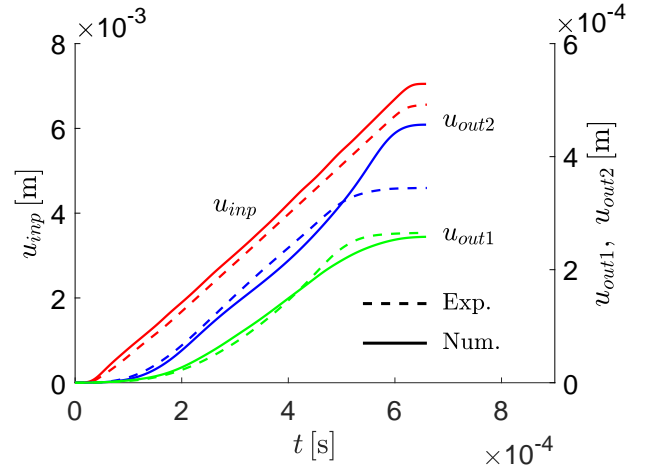
(a) Incident (ε_{inc}) and reflected (ε_{ref}) strains.



(b) Transmitted strains (ε_{tr1} , ε_{tr2}).



(c) Interface velocities.



(d) Displacements of the input interface (u_{inp} , left scale) and of the two output interfaces (u_{out1} and u_{out2} , right scale).

Figure 12: Experimental and numerical quantities (strains, velocities, displacements) at the bars-rib interfaces.

The signals presented in Fig. 12 were obtained during a test where fracture occurred before equilibrium. The striker velocity was 17.39 m/s both in the experiment and in the simulation. For this test, the experimental force histories are plotted in Fig. 9e.

The numerical strain signals were post processed through a MATLAB subroutine to calculate the forces at interfaces with the porcine rib using Eq. (2a), Eq. (2b) and Eq.(2c). In order to be coherent with the experimental procedure, this MATLAB subroutine applies an appropriate time shifting procedure to the numerical strains. The obtained incident, reflected and transmitted waves are plotted in Fig. 12a and 12b respectively. The velocity v_{inp} and the displacement u_{inp} of the input bar-rib sample are plotted in Fig. 12c and 12d.

A keen observation to the ε_{inc} and ε_{ref} , reveals that there is a slight difference between numerical and experimental signals. On the other hand, the difference in the transmitted strain signals can be explained by the difference in geometry. Yet, the numerical interface velocities and displacements are almost similar to that of experimental.

The numerical displacement of output interface 2 shows a peculiar response. It is clear that it superposes with experimental signal till $t \approx 500 \times 10^{-4}$ s. Beyond this point of time the magnitude of u_{out2} Num. is greater than u_{out2} Exp., that can be explained by the loss of contact between the sample and output bar interface 2 in the simulation (see Fig. 11). One has to recall that the experimental samples were sanded at the anterior posterior ends to establish a good contact at the sample-output bar interface. Rather, the numerical sample was kept as natural as possible in order to avoid unnecessary penetration and unwanted noise in the strain signals and contact force. In Fig. 10 a crack starts to propagate towards the input bar-sample interface until rupture at $t' = 2.30 \times 10^{-3}$ s. This time translates to $t \approx 4.50 \times 10^{-4}$ s in Fig. 12d, at which the numerical sample is no more in contact with output bar 2. The increase in displacement beyond this time represents the rigid displacement of output bar.

6.3. Consistency of predictions of force vs. time response

The contact force history is highly sensible on the contact algorithm. If the simulated contact correctly represents its physical counterpart, the reaction force between the sample and the input bar obtained either through the strain signals or directly by the contact algorithm must be similar. The forces calculated using these two methods are presented in Fig. 13.

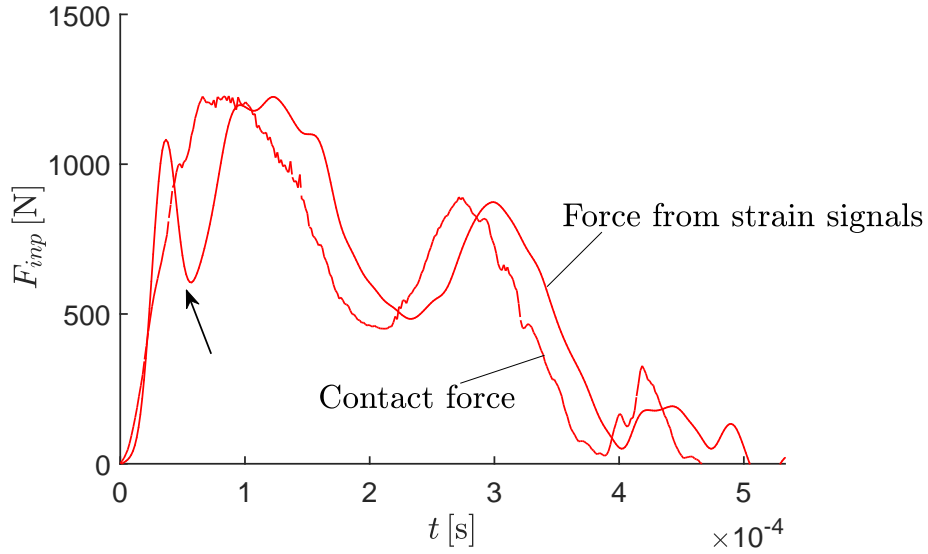


Figure 13: Comparison of numerical forces obtained from the strain histories (solid line) and directly from the contact algorithm (dashed line)

Two keen observations can be made from Fig. 13:

(i) The arrow in Fig. 13 indicates fluctuation of the force which arises due to an accuracy issue of the time shifting procedure (in the determination of the origin time t'_0 to be precise). It is a well known issue of the SHPB experiments.

(ii) there is a time lag of about 0.19×10^{-3} s between the force form contact and force from strain signals. Recalling that the formula used to process the SHPB signals assume a total contact at each bar interface. In reality, the sample does not stay in contact with the total bar cross-section as illustrated in Fig. 14. Therefore, the more planar the contact surface, the less is the discrepancy between these forces.

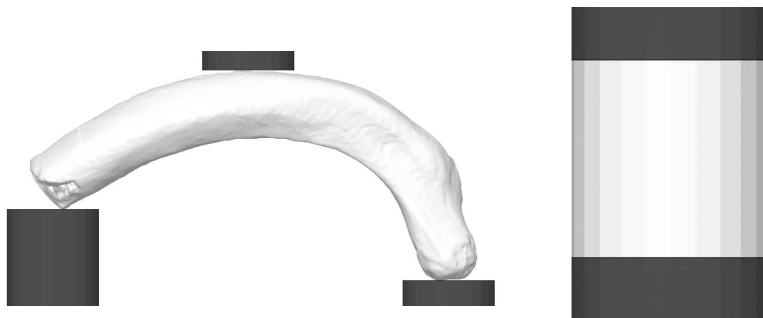


Figure 14: Influence of contact surface. Left: bending rib model. Right: pure compression model (SHPB test).

Fig. 14 presents the aforementioned difference in contact surface between the entire rib

sample and a cylindrical rib bone sample.

If the surfaces at the sample-input bar interface are of similar geometrical definition this time difference should be zero.

In addition, if the contact algorithm is physically and numerically veracious, the forces amplitude should be the same. These two exigencies are satisfied if the bar-sample interface area is made equal to the bar cross-section in a pure compressive test (SHPB) simulation. It can be seen that the force response from strain strain signals (solid line) and that obtained directly from contact (dashed line) superimpose.

The highest discrepancy noted in the present simulation (rib) is represented in Fig. 13.

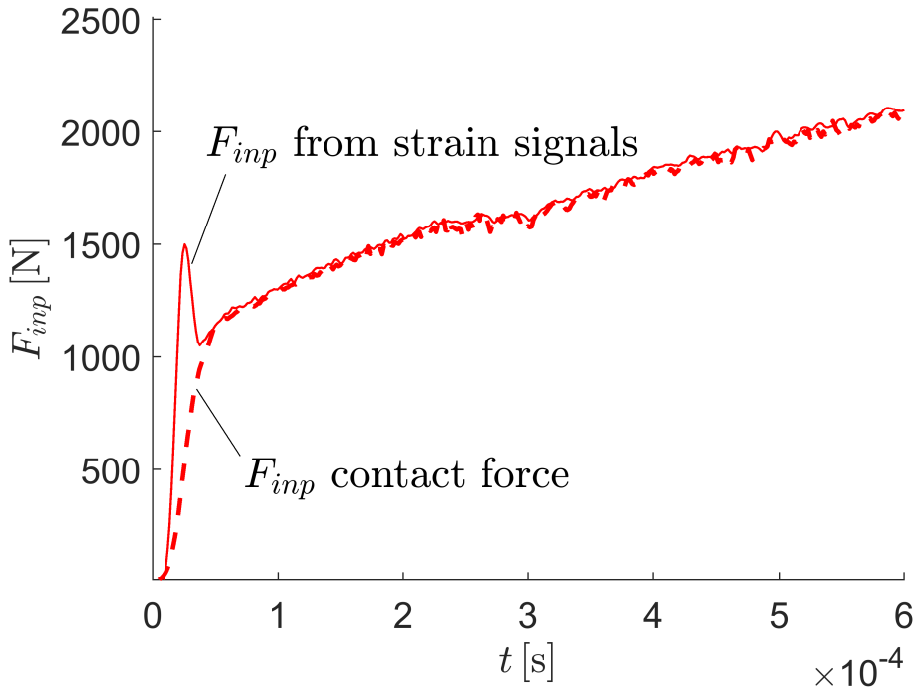


Figure 15: Comparison of Numerical Force data in the pure compression simulation.

In fact, care must be taken to compare the numerical results with the experimental data of similar characteristics, in this case, the time taken for fracture was considered as the control variable. As the numerical $t_{frac} \approx 0.512 \times 10^{-3} s$, all the simulation data were compared with test with fracture during non-equilibrium phase in Sec. 5.1.

It is evident that there would always be a difference between the numerical force response and experimental force response since it is not possible to use the same sample for numerical and experimental purposes due to the drying process.

6.4. Comparison of numerical and experimental force displacement response

The structure behaves initially as an elastic body. At small times, the response is determined only by the material properties and the local stiffness distribution near the impact area. Therefore, during this time interval (on the left of the vertical dotted line in Fig. 16), the form of the response histories at the very beginning are similar for every numerical cases.

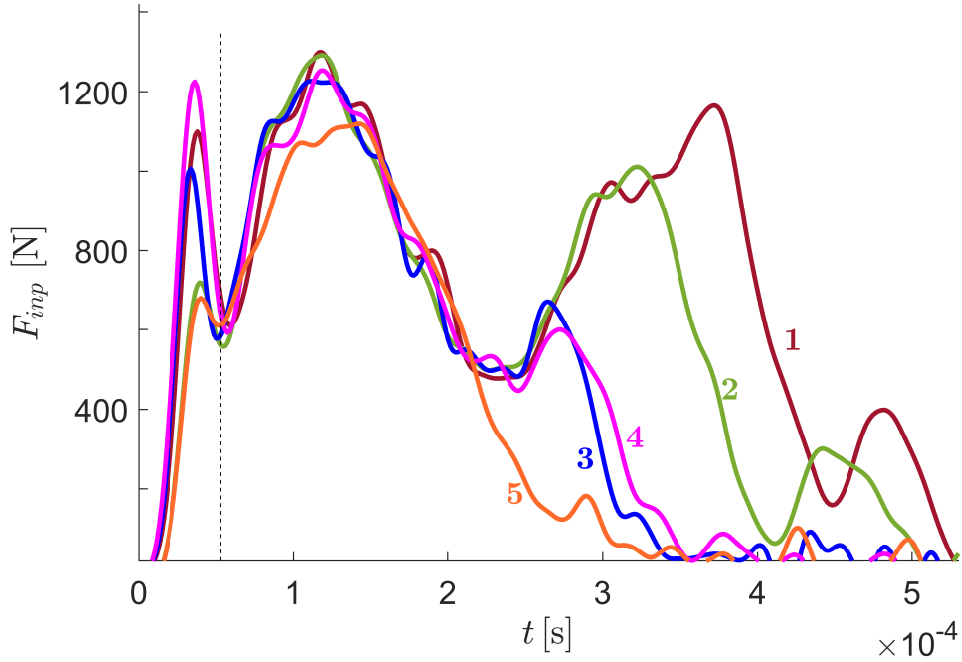


Figure 16: Numerical F_{imp} vs. t response corresponding to different $\varepsilon_{fd}/\varepsilon_{fs}$ curves tested (see Fig. 6b)

The numerical simulation was carried out with a striker velocity of 17.39 m/s, leading to a numerical interface velocity V of 10.46 m/s. The numerical results are compared to an experimental case of similar conditions *i.e.* Corridor-3. The best numerical result corresponds to that obtained with input curve 2 (Fig. 6b) of the damage law and is shown in Fig. 17.

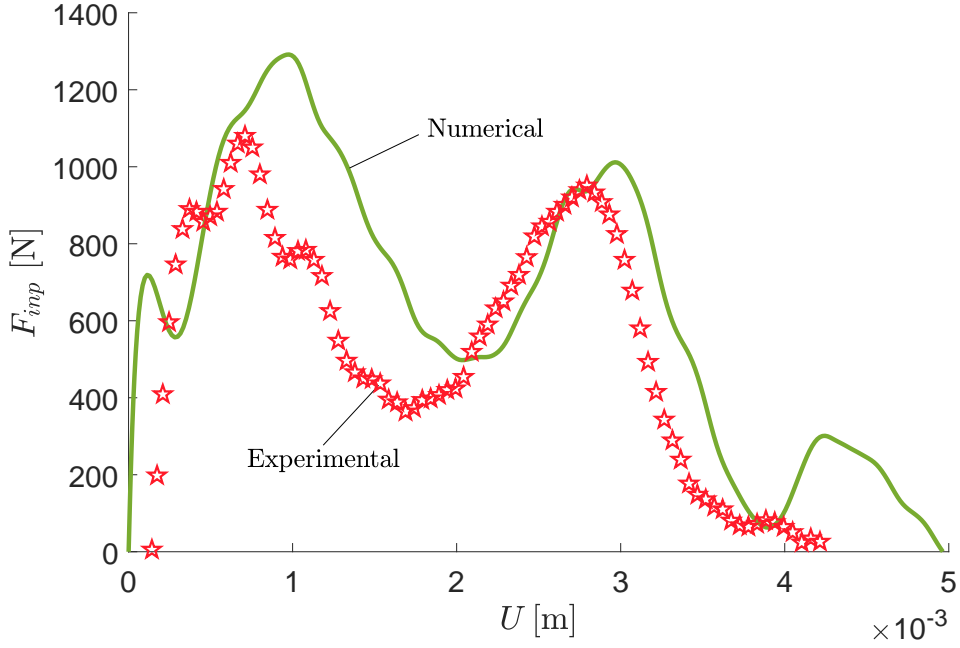


Figure 17: Comparison with experimental response.

The differences between experimental and numerical response arise due to the difference in the geometry of samples tested.

7. Conclusion

The present study provides both experimental and numerical evidence for fracture propagation in ribs under certain dynamics impact environments.

The dynamic three-point bending split Hopkinson bar had led to the measurements of dynamic physical quantities characterizing the rib fracture.

Three types of responses were observed in our experiments, (i) no fracture, (ii) fracture during equilibrium between external forces and (iii) fracture before equilibrium was established.

Thanks to the High-Resolution peripheral Quantitative Computer Tomography technique and the current image resolution, it is possible to obtain an accurate geometrical and material representation of the rib. The geometrical description permits to construct a FE model including the distribution of different parts. The apparent density is correctly correlated with grey scale of bone. As in previous studies in the literature, mechanical properties (Young modulus, yield stress, ultimate stress, strain at fracture) were correlated with apparent density. The present study proves that this methodology provides an appropriate simulation of the fracture process.

Also the numerical values belong in the range found by previous authors.

Concerning the numerical simulations, the current study indicates successful FE implementation of complicated constitutive and damage law with the consideration of strain rate effects and non-linear damage accumulation.

Even though the correlation between the experimental and numerical fracture pattern is adequate, an accurate representation of a more realistic fracture behavior requires model improvements such as: bone heterogeneity, transmission of forces between the different constituents of the rib. Moreover, optimization of the damage law parameters through respective experimental data, will further improve the efficiency of the proposed FE model.

The porcine rib was used as a human surrogate rib in order to develop an adapted methodology for the human rib. The improved human rib model will be implemented in numerical human body model.

8. Acknowledgments

The authors acknowledge the french Region Centre-Val de Loire for having provided the funds for the study. The authors would also thank Dr. Eric Lespessaille (MD, PhD, PAST) of Orleans Regional Hospital, for his valuable assistance in HR-pQCT procedure.

References

- Abdel-Wahab, A. A. and V. V. Silberschmidt (2011). Numerical modelling of impact fracture of cortical bone tissue using X-FEM. *Journal of Theoretical and Applied Mechanics Vol. 49 nr 3*, 599–619.
- Arnoux, P., S. Jooneknidt, L. Tholon, and K. Kayvantash (2003, January). Radioss finite element model of the Thor dummy. *International Journal of Crashworthiness 8(6)*, 529–541.
- Arunan, Y. and B. Roodenburg (2017, August). Chest trauma. *Anaesthesia & Intensive Care Medicine 18(8)*, 390–394.
- Aubert, R., J. Pavier, N. Eches, A. Langlet, and P. Bailly (2012, September). On the use of Hopkinson bar-bending apparatus to study soft impact on porcine ribs. *Computer Methods in Biomechanics and Biomedical Engineering 15(sup1)*, 311–312.
- Bessho, M., I. Ohnishi, J. Matsuyama, T. Matsumoto, K. Imai, and K. Nakamura (2007). Prediction of strength and strain of the proximal femur by a CT-based finite element method. *Journal of Biomechanics 40(8)*, 1745–1753.
- Burnside, N. and K. McManus (2014, May). Blunt thoracic trauma. *Surgery (Oxford) 32(5)*, 254–260.
- Burstein, A. H., J. M. Zika, K. G. Heiple, and L. Klein (1975, October). Contribution of collagen and mineral to the elastic-plastic properties of bone. *The Journal of Bone and Joint Surgery. American Volume 57(7)*, 956–961.
- Carter, D. R. and W. C. Hayes (1977, October). The compressive behavior of bone as a two-phase porous structure. *The Journal of Bone and Joint Surgery. American Volume 59(7)*, 954–962.
- Cavanaugh, J. M., Y. Zhu, Y. Huang, and A. I. King (1993, November). Injury and Response of the Thorax in Side Impact Cadaveric Tests. SAE Technical Paper 933127, SAE International, Warrendale, PA.
- Charpail, E. (2006, January). *Analyse du comportement mécanique des côtes humaines en dynamique*. Phd thesis, Paris, ENSAM.

- Currey, J. D. (1969, March). The mechanical consequences of variation in the mineral content of bone. *Journal of Biomechanics* 2(1), 1–11.
- Dall’Ara, E., B. Luisier, R. Schmidt, F. Kainberger, P. Zysset, and D. Pahr (2013, January). A nonlinear QCT-based finite element model validation study for the human femur tested in two configurations in vitro. *Bone* 52(1), 27–38.
- Delvare, F., J. Hanus, and P. Bailly (2010). A non-equilibrium approach to processing hopkinson bar bending test data: Application to quasi-brittle materials. *International Journal of Impact Engineering* 37(12), 1170 – 1179.
- Doblaré, M., J. M. García, and M. J. Gómez (2004, September). Modelling bone tissue fracture and healing: a review. *Engineering Fracture Mechanics* 71(13), 1809–1840.
- Fallouh, H., R. Dattani-Patel, and S. Rathinam (2017). Blunt thoracic trauma. *Surgery (Oxford)* 35(5), 262 – 268.
- Fillipe, A., F. Markus, and H. André (2014). On the prediction of Damage and Failure in LS-DYNA: A comparison of GISSMO and DIEM. In *Constitutive Modelling*, Bamberg, Germany, pp. 1–12. DYNAmore GmbH.
- Flanagan, D. P. and T. Belytschko (1981). A uniform strain hexahedron and quadrilateral with orthogonal hourglass control. *International Journal for Numerical Methods in Engineering* 17(5), 679–706.
- Frieder, N., F. Markus, and H. André (2009). Considering damage history in Crashworthiness simulations. Stuttgart, Germany, pp. 1–10. DYNAmore GmbH.
- Garcia, D. (2006). *Elastic plastic damage laws for cortical bone*. Ph. D. thesis, Ecole Polytechnique Fédérale de Laussane, Laussane, Switzerland.
- Gary, G. (2005). David – instruction manual. *tech. rep., LMS, Ecole Polytechnique – France*.
- Gibson, L. J. (1985). The mechanical behaviour of cancellous bone. *Journal of Biomechanics* 18(5), 317 – 328.
- Hambli, R. (2011a, August). Apparent damage accumulation in cancellous bone using neural networks. *Journal of the Mechanical Behavior of Biomedical Materials* 4(6), 868–878.

- Hambli, R. (2011b). Multiscale prediction of crack density and crack length accumulation in trabecular bone based on neural networks and finite element simulation. *International Journal for Numerical Methods in Biomedical Engineering* 27(4), 461–475.
- Hambli, R. (2013, October). Micro-CT finite element model and experimental validation of trabecular bone damage and fracture. *Bone* 56(2), 363–374.
- Haug, E., H.-Y. Choi, S. Robin, and M. Beaugonin (2004, January). Human Models for Crash and Impact Simulation. In *Handbook of Numerical Analysis, Volume 12 of Computational Models for the Human Body*, pp. 231–452. Elsevier.
- Horst, K., H. Andruszkow, C. D. Weber, M. Pishnamaz, C. Herren, Q. Zhi, M. Knoke, R. Lefering, F. Hildebrand, and H.-C. Pape (2017, October). Thoracic trauma now and then: A 10 year experience from 16,773 severely injured patients. *PLOS ONE* 12(10), e0186712.
- Johnson, T. P. M., S. Socrate, and M. C. Boyce (2010, October). A viscoelastic, viscoplastic model of cortical bone valid at low and high strain rates. *Acta Biomaterialia* 6(10), 4073–4080.
- Karkar, M. (2017, November). *Personnalisation morpho-mécanique de la voûte crânienne humaine à différentes vitesses de sollicitations*. PhD Thesis, Valenciennes.
- Keaveny, T. M., E. F. Wachtel, and D. L. Kopperdahl (1999, May). Mechanical behavior of human trabecular bone after overloading. *Journal of Orthopaedic Research: Official Publication of the Orthopaedic Research Society* 17(3), 346–353.
- Kelly, N. and J. P. McGarry (2012, May). Experimental and numerical characterisation of the elasto-plastic properties of bovine trabecular bone and a trabecular bone analogue. *Journal of the Mechanical Behavior of Biomedical Materials* 9, 184–197.
- Keyak, J. H., I. Y. Lee, and H. B. Skinner (1994, November). Correlations between orthogonal mechanical properties and density of trabecular bone: use of different densitometric measures. *Journal of Biomedical Materials Research* 28(11), 1329–1336.
- Kopperdahl, D. L. and T. M. Keaveny (1998, July). Yield strain behavior of trabecular bone. *Journal of Biomechanics* 31(7), 601–608.

- Li, Z., M. W. Kindig, J. R. Kerrigan, C. D. Untaroiu, D. Subit, J. R. Crandall, and R. W. Kent (2010, January). Rib fractures under anterior-posterior dynamic loads: experimental and finite-element study. *Journal of Biomechanics* 43(2), 228–234.
- Liman, S. T., A. Kuzucu, A. I. Tastepe, G. N. Ulasan, and S. Topcu (2003, March). Chest injury due to blunt trauma. *European Journal of Cardio-Thoracic Surgery* 23(3), 374–378.
- Maeno, T. and J. Hasegawa (2001, June). Development of a Finite Element Model of the Total Human Model for Safety (thums) and Application to Car-Pedestrian Impacts. SAE Technical Paper 2001-06-0054, SAE International, Warrendale, PA.
- Malik, C. L., S. M. Stover, R. B. Martin, and J. C. Gibeling (2003, February). Equine cortical bone exhibits rising R-curve fracture mechanics. *Journal of Biomechanics* 36(2), 191–198.
- McElhaney, J. H. (1966, July). Dynamic response of bone and muscle tissue. *Journal of Applied Physiology* 21(4), 1231–1236.
- Merle, R. and H. Zhao (2006). On the errors associated with the use of large diameter shpb, correction for radially non-uniform distribution of stress and particle velocity in shpb testing. *International Journal of Impact Engineering* 32(12), 1964 – 1980.
- Rice, J. C., S. C. Cowin, and J. A. Bowman (1988, January). On the dependence of the elasticity and strength of cancellous bone on apparent density. *Journal of Biomechanics* 21(2), 155–168.
- Robin, S. (2001, June). HUMOS: Human model for safety~A joint effort towards the development of refined human-like car occupant models. SAE Technical Paper 2001-06-0129, SAE International, Warrendale, PA.
- Ruiz, C. and R. Mines (1985). The hopkinson pressure bar: an alternative to the instrumented pendulum for charpy tests. *Int J Fract* 29(2), 101–109.
- Schaffler, M. B. and D. B. Burr (1988). Stiffness of compact bone: effects of porosity and density. *Journal of Biomechanics* 21(1), 13–16.
- Schoell, S. L., A. A. Weaver, N. A. Vavalle, and J. D. Stitzel (2015). Age- and sex-specific thorax finite element model development and simulation. *Traffic Injury Prevention* 16 Suppl 1, S57–65.

- Shen, F., T. E. Tay, J. Z. Li, S. Nigen, P. V. Lee, and H. K. Chan (2006, October). Modified Bilston nonlinear viscoelastic model for finite element head injury studies. *Journal of biomechanical engineering* 128(5), 797–801.
- Shirley, P. J. (2005, July). Trauma and critical care III: chest trauma. *Trauma* 7(3), 133–142.
- Taylor, D. and T. Lee (2003, August). Microdamage and mechanical behaviour: predicting failure and remodelling in compact bone. *Journal of Anatomy* 203(2), 203–211.
- Taylor, W. R., E. Roland, H. Ploeg, D. Hertig, R. Klabunde, M. D. Warner, M. C. Hobatho, L. Rakotomanana, and S. E. Clift (2002, June). Determination of orthotropic bone elastic constants using FEA and modal analysis. *Journal of Biomechanics* 35(6), 767–773.
- Teo, J. C., K. M. Si-Hoe, J. E. Keh, and S. H. Teoh (2006). Relationship between ct intensity, micro-architecture and mechanical properties of porcine vertebral cancellous bone. *Clinical Biomechanics* 21(3), 235 – 244.
- Ural, A. and D. Vashishth (2007, October). Effects of intracortical porosity on fracture toughness in aging human bone: a microCT-based cohesive finite element study. *Journal of Biomechanical Engineering* 129(5), 625–631.
- Vashishth, D., K. E. Tanner, and W. Bonfield (2003, January). Experimental validation of a microcracking-based toughening mechanism for cortical bone. *Journal of Biomechanics* 36(1), 121–124.
- Vose, G. P. and A. L. Kubala (1959). Bone strength-its relationship to X-ray-determined ash content. *Human Biology* 31, 261–270.
- Wolfram, U. and S. Jakob (2016, August). Post-yield and failure properties of cortical bone. *BoneKey reports* 5(829).
- Wolfram, U., H.-J. Wilke, and P. K. Zysset (2011, April). Damage accumulation in vertebral trabecular bone depends on loading mode and direction. *Journal of Biomechanics* 44(6), 1164–1169.
- Wood, J. L. (1971, January). Dynamic response of human cranial bone. *Journal of Biomechanics* 4(1), 1–12.

- Yates, K. and C. Untaroiu (2018). Subject-Specific Modeling of Human Ribs: Finite Element Simulations of Rib Bending Tests, Mesh Sensitivity, Model Prediction with Data Derived From Coupon Tests. In *15th International LS Dyna User's Conference proceedings*, Detroit, Michigan, USA, pp. 7.
- Zhao, H. and G. Gary (1995). A three dimensional analytical solution of the longitudinal wave propagation in an infinite linear viscoelastic cylindrical bar. application to experimental techniques. *Journal of the Mechanics and Physics of Solids* 43(8), 1335 – 1348.
- Zhao, H., G. Gary, and J. R. Klepaczko (1997, April). On the use of a viscoelastic split hopkinson pressure bar. *International Journal of Impact Engineering* 19(4), 319–330.
- Zioupos, P., U. Hansen, and J. D. Currey (2008, October). Microcracking damage and the fracture process in relation to strain rate in human cortical bone tensile failure. *Journal of Biomechanics* 41(14), 2932–2939.